Int. J. Solids Structures Vol. 27, No. 12, pp. 1515–1535, 1991
Printed in Great Britain.

0020-7683/91 $3.00 + .00

ANALYSIS OF A ZIG-ZAG ARRAY OF CIRCULAR INCLUSIONS IN A SOLID UNDER UNIAXIAL TENSION

M. ISIDA and H. IGAWA
Department of Mechanical Engineering, Kurume Institute of Technology,
2228 Kamitsu-machi, Kurume 830, Japan

(*Received* 18 *July* 1989; *in revised form* 23 *March* 1990)

Abstract—This paper is concerned with a theoretical analysis of an infinite zig-zag array of circular inclusions in an infinite solid under uniaxial tension. We take properly defined unit regions, assume the complex stress potentials to be in the form of Laurent and Taylor series expansions, and determine the unknown coefficients from the boundary conditions for the unit regions. Numerical results for the interface stresses and the effect of inclusions on the tensile stiffness of the solid are given for various combinations of the mechanical and geometric parameters. The results are fitted to reliable polynomial formulae for the convenience of engineering applications.

1. INTRODUCTION

A zig-zag array of circular inclusions is quite important, not only as an ordinary stress concentration problem, but also as a model of randomly distributed inclusions in materials. The purpose of this paper is to give a near exact solution for an infinite zig-zag array of circular inclusions in an infinite solid under uniaxial tension, and to examine the effects of the size, location and rigidity of the inclusions on the interface stresses and tensile stiffness of the solid.

This problem is treated by generalizing the previous analysis of an infinite zig-zag array of circular holes (Isida and Igawa, 1991). We choose suitable unit regions, and assume Laurent and Taylor series expansions for the complex stress potentials in forms satisfying the continuity relations along the inclusion boundaries. The unknown coefficients in these series are determined from the boundary conditions at the outer edges of the unit regions. At this stage, we use a new procedure based on elementwise resultant forces and displacements which was developed by Isida (1971) in order to get highly accurate results.

Numerical calculations are carried out for various combinations of mechanical and geometric parameters. Results for the interface stresses and tensile stiffness of the solid are represented in tables and figures, and are fitted to reliable polynomial formulae for convenience in engineering applications.

2. THEORETICAL ANALYSIS

2.1. *Fundamental equations and description of problem*

In plane elasticity, all the physical quantities are given in terms of two complex potentials $\phi(z)$, $\psi(z)$ and their derivatives, where $z = x+iy$ (Timoshenko and Goodier, 1951).

Components of stress:

$$\sigma_y + \sigma_x = 4\,\mathrm{Re}\,[\phi'(z)] \tag{1.1}$$

$$\sigma_y - \sigma_x + 2i\tau_{xy} = 2[\bar{z}\phi''(z) + \psi'(z)]. \tag{1.2}$$

Components of resultant force:

$$P_y + iP_x = -\bar{\phi}(\bar{z}) - \bar{z}\phi'(z) - \psi(z) + (\text{an arbitrary constant}). \tag{2}$$

Components of displacement:

$$2G(u-iv) = \kappa\bar{\phi}(\bar{z}) - z\phi'(z) - \psi(z) + (\text{an arbitrary constant}), \tag{3}$$

where G is the shear modulus and κ is defined by Poisson's ratio ν as

$$\kappa = \begin{cases} \dfrac{3-\nu}{1+\nu} & (\text{plane stress}) \\ 3-4\nu & (\text{plane strain}). \end{cases} \tag{4}$$

Constant terms in eqns (2) and (3) depend on the starting points from which P_r, P_s and u, v are measured, but they are unessential in the analysis.

We also have the following expressions for the stresses in polar coordinates:

$$\sigma_\theta + \sigma_r = 4\,\mathrm{Re}\,[\phi'(z)] \tag{5.1}$$

$$\sigma_\theta - \sigma_r + 2i\tau_{r\theta} = 2\,e^{2i\theta}\,[\bar{z}\phi''(z) + \psi'(z)]. \tag{5.2}$$

This paper deals with an infinite solid containing an infinite zig-zag array of circular inclusions. Let the radius of the inclusions be a, and the spacings between adjacent inclusions in horizontal and vertical rows be $2b$ and $2c$, respectively, as shown in Fig. 1. The x- and y-axes are taken with their origin at the center of one of the inclusions, and the solid is subjected to an average tensile stress σ in the y-direction. Figures 12(a) and 12(b) of Section 3.4 show the two typical arrays of inclusions corresponding to $c/b = 1$ and $\sqrt{3}$, which are the square array and the equilateral triangular array, respectively.

2.2. *Complex stress potentials*

We take a proper unit region and express the complex stress potentials in forms satisfying the symmetry conditions as well as the traction-free conditions along the inclusion boundary. We then determine the unknown coefficients in the stress potentials from the boundary conditions at the outer edges of the unit region.

For the above unit region, we use the triangle ODFO or the rectangle ODHKO shown in Fig. 1, as in the previous analysis of a zig-zag array of circular holes (Isida and Igawa, 1991). Usually the triangular region is more simple and convenient than the rectangular region, but the latter is also used for large values of c/b since the triangular region gives poor results.

We denote the domains of the matrix and inclusion in the unit region by (I) and (II), respectively, and denote the shear moduli, Poisson's ratios, Young's moduli and the values

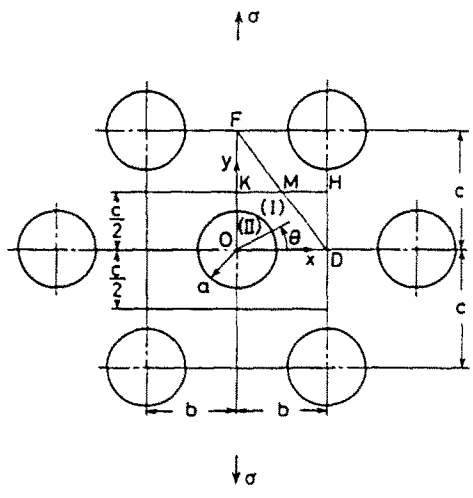

Fig. 1. Infinite zig-zag array of circular inclusions in infinite solid subjected to tension.

of κ of these domains by $G_{\rm I}$, $\nu_{\rm I}$, $E_{\rm I}$, $\kappa_{\rm I}$ and $G_{\rm II}$, $\nu_{\rm II}$, $E_{\rm II}$, $\kappa_{\rm II}$, respectively. We also define the dimensionless rigidity of the inclusions as follows:

$$\Gamma = \frac{G_{\rm II}}{G_{\rm I}}. \tag{6}$$

$\Gamma = 0$ and $\Gamma = \infty$ correspond to holes and rigid inclusions, respectively, and the present analysis is valid in the whole range of Γ including these special cases.

We now write the stress potentials $\phi_{\rm I}(z)$, $\psi_{\rm I}(z)$ and $\phi_{\rm II}(z)$, $\psi_{\rm II}(z)$ for domains (I) and (II) in proper expanded forms. $\phi_{\rm II}(z)$ and $\psi_{\rm II}(z)$ must be analytic in domain (II), and they are expressed in the following Taylor series:

$$\phi_{\rm II}(z) = \sum_{n=0}^{\infty} k_{2n} z^{2n+1} \tag{7.1}$$

$$\psi_{\rm II}(z) = \sum_{n=0}^{\infty} l_{2n} z^{2n+1}. \tag{7.2}$$

Note that symmetry dictates that all of the even power terms are missing and that the coefficients k_{2n} and l_{2n} are real in the above expressions.

The stress potentials for domain (I) may contain singularities inside the inclusion, and they can be written as the following Laurent series:

$$\phi_{\rm I}(z) = \sum_{n=0}^{\infty} (K_{2n} z^{2n+1} + F_{2n} z^{-2n-1}) \tag{8.1}$$

$$\psi_{\rm I}(z) = \sum_{n=0}^{\infty} (L_{2n} z^{2n+1} + H_{2n} z^{-2n-1}). \tag{8.2}$$

Even power terms are missing and all the coefficients are real for the same reason as for eqns (7).

2.3. *Boundary conditions along inclusion*

By using eqns (7) and (8) in eqns (2) and (3), the resultant forces and displacements for domains (I) and (II) are given as follows:

$$P_{x\rm I} + {\rm i}P_{y\rm I} = -\sum_{n=0}^{\infty} (K_{2n} z^{2n+1} + F_{2n} z^{-2n-1}) - z \sum_{n=0}^{\infty} (2n+1)(K_{2n} z^{2n} - F_{2n} z^{-2n-2}) - \sum_{n=0}^{\infty} (L_{2n} z^{2n+1} + H_{2n} z^{-2n-1}) \tag{9.1}$$

$$P_{x\rm II} + {\rm i}P_{y\rm II} = -\sum_{n=0}^{\infty} k_{2n} z^{2n+1} - z \sum_{n=0}^{\infty} (2n+1) k_{2n} z^{2n} - \sum_{n=0}^{\infty} l_{2n} z^{2n+1} \tag{9.2}$$

$$2G_{\rm I}(u_{\rm I} - {\rm i}v_{\rm I}) = \kappa_{\rm I} \sum_{n=0}^{\infty} (K_{2n} z^{2n+1} + F_{2n} z^{-2n-1}) - z \sum_{n=0}^{\infty} (2n+1)(K_{2n} z^{2n} - F_{2n} z^{-2n-2}) - \sum_{n=0}^{\infty} (L_{2n} z^{2n+1} + H_{2n} z^{-2n-1}) \tag{9.3}$$

$$2G_{\rm II}(u_{\rm II} - {\rm i}v_{\rm II}) = \kappa_{\rm II} \sum_{n=0}^{\infty} k_{2n} z^{2n+1} - z \sum_{n=0}^{\infty} (2n+1) k_{2n} z^{2n} - \sum_{n=0}^{\infty} l_{2n} z^{2n+1}. \tag{9.4}$$

Arbitrary constants may be added to the right-hand sides of eqns (9.1)–(9.4), as shown by eqns (2) and (3), but they are put to zero by assigning the conditions that $P_{x\rm I} = P_{x\rm II} = 0$ along the x-axis, $P_{y\rm I} = P_{y\rm II} = 0$ along the y-axis and $v_{\rm I} = v_{\rm II} = 0$ along the x-axis, $u_{\rm I} = u_{\rm II} = 0$ along the y-axis.

The above expressions must satisfy the continuity conditions for the stress and dis-

placement along the inclusion boundary, that is, along $z = a\,e^{i\theta}$ and for any θ

$$P_{xI}+iP_{yI} = P_{xII}+iP_{yII}, \quad u_I - iv_I = u_{II} - iv_{II}. \tag{10}$$

Equations (9.1)–(9.4), together with eqns (10), give the following relations among the coefficients in the complex potentials (7) and (8):

$$H_0 = 2\left(\frac{\Gamma(\kappa_I+1)}{2\Gamma+\kappa_{II}-1} - 1\right)a^2K_0 \tag{11.1}$$

$$H_{2n} = \frac{\Gamma-1}{\Gamma\kappa_I+1}(2n-1)a^{4n}L_{2n-2} + \left(\frac{\Gamma-1}{\Gamma\kappa_I+1}(4n^2-1) + \frac{\Gamma\kappa_I-\kappa_{II}}{\Gamma+\kappa_{II}}\right)a^{4n+2}K_{2n} \quad (n \geq 1) \tag{11.2}$$

$$F_{2n-2} = \frac{\Gamma-1}{\Gamma\kappa_I+1}[a^{4n-2}L_{2n-2} + (2n+1)a^{4n}K_{2n}] \quad (n \geq 1) \tag{11.3}$$

$$k_0 = \frac{\Gamma(\kappa_I+1)}{2\Gamma+\kappa_{II}-1}K_0, \quad k_{2n} = \frac{\Gamma(\kappa_I+1)}{\Gamma+\kappa_{II}}K_{2n} \quad (n \geq 1) \tag{11.4}$$

$$l_{2n-2} = \frac{\Gamma(\kappa_I+1)}{\Gamma\kappa_I+1}L_{2n-2} + \Gamma(\kappa_I+1)\left(\frac{1}{\Gamma\kappa_I+1} - \frac{1}{\Gamma+\kappa_{II}}\right)(2n-1)a^2K_{2n} \quad (n \geq 1). \tag{11.5}$$

Inserting eqns (11.1)–(11.3) into eqns (8), $\phi_I(z)$ and $\psi_I(z)$ are reduced to the forms containing independent unknowns K_{2n} and L_{2n}. Equations (11.4) and (11.5) give the coefficients in $\phi_{II}(z)$ and $\psi_{II}(z)$ for domain (II), after K_{2n} and L_{2n} in $\phi_I(z)$ and $\psi_I(z)$ have been determined.

2.4. *Boundary conditions and determination of unknowns*

As shown in the preceding section, the complex potentials (8), rewritten in terms of the independent unknowns K_{2n} and L_{2n} using eqns (11.1)–(11.3), completely satisfy the continuity conditions along the inclusion boundary as well as the symmetry conditions. Therefore, the unknowns K_{2n} and L_{2n} must be determined only from the boundary conditions along the outer edges of the unit region.

For the numerical calculation, we use a method based on elementwise resultant forces and displacements. This method was developed by Isida (1971) and proved a powerful technique in analysing various problems of multi-connected domains (Isida, 1978; Isida and Noguchi, 1984). The procedures for both the unit regions ODFO and ODHKO shown in Fig. 1 are fully described in a previous analysis on circular holes (Isida and Igawa, 1991). In the present paper, the procedure for only the triangular region will be stated.

Referring to Fig. 2, let M be the midpoint of the side DF of the triangular unit region ODFO. Then the stress field is symmetric about point M, and any two points S_1 and S_2 on DF which are equally distant from M must be in the same stress state and the displacements of these points relative to M must be the same. In order to take advantage of these conditions in numerical computations, we divide the side DF into N equal intervals Q_1Q_2, $Q_2Q_3, \ldots, Q_NQ_{N+1}$, where N is an even integer, $N = 2m$.

First, the two points Q_t and Q_{2m+2-t} $(t = 1, 2, \ldots, m)$ which are equally distant from the point M or Q_{m+1} should be in the same stress state. This requires the following conditions on the resultant forces:

$$[P_{xI}]_{Q_t}^{Q_{m+1}} = [P_{xI}]_{Q_{m+1}}^{Q_{2m+2-t}}, \tag{12.1}$$

$$[P_{yI}]_{Q_t}^{Q_{m+1}} = [P_{yI}]_{Q_{m+1}}^{Q_{2m+2-t}} \quad (t = 1, 2, \ldots, m;\ m = N/2). \tag{12.2}$$

Secondly, the equality of the displacements at Q_t and Q_{2m+2-t} relative to M requires

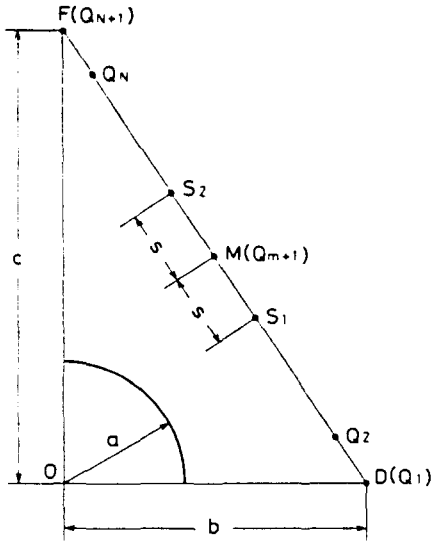

Fig. 2. Triangular unit region.

that

$$[u_1]_{Q_t}^{Q_{m+1}} = [u_1]_{Q_{m+1}}^{Q_{2m+2-t}} \tag{13.1}$$

$$[v_1]_{Q_t}^{Q_{m+1}} = [v_1]_{Q_{m+1}}^{Q_{2m+2-t}} \quad (t = 1, 2, \ldots, m; m = N/2). \tag{13.2}$$

In eqns (12) and (13), the symbol $[\ ]_A^B$ denotes the difference in the values of the quantity within the brackets at points B and A.

Furthermore, the resultant forces along the side DF should balance the external load,

$$[P_{x1}]_D^F = 0, \quad [P_{y1}]_D^F = \sigma b. \tag{14}$$

Thus we have $(2N+2)$ boundary relations given by eqns (12)–(14) for the independent coefficients K_{2n} and L_{2n} in the complex potentials (8). Corresponding to these relations, we take K_{2n} and L_{2n} $(n = 0, 1, 2, \ldots, N)$ as the unknowns neglecting higher order coefficients, and they are determined from the above boundary conditions.

2.5. *Small inclusions*

We consider the special case when the inclusions are extremely small. It can be treated as a single inclusion in an infinite solid. In this case, the stress state at infinity gives the following expressions for the coefficients K_{2n} and L_{2n} in the complex potentials (8):

$$K_0 = \frac{\sigma}{4}, \quad L_0 = \frac{\sigma}{2}, \quad K_{2n} = L_{2n} = 0 \quad (n \geqslant 1) \tag{15}$$

which yield from eqns (11.1)–(11.5)

$$H_0 = \frac{\sigma}{2}\left(\frac{\Gamma(\kappa_1+1)}{2\Gamma+\kappa_{II}-1} - 1\right)a^2, \quad H_2 = \frac{\sigma}{2}\frac{\Gamma-1}{\Gamma\kappa_1+1}a^4, \quad H_{2n} = 0 \quad (n \geqslant 2) \tag{16.1}$$

$$F_0 = \frac{\sigma}{2}\frac{\Gamma-1}{\Gamma\kappa_1+1}a^2, \quad F_{2n} = 0 \ (n \geqslant 1) \tag{16.2}$$

and

$$k_0 = \frac{\sigma}{4}\frac{\Gamma(\kappa_1+1)}{2\Gamma+\kappa_{II}-1}, \quad l_0 = \frac{\sigma}{2}\frac{\Gamma(\kappa_1+1)}{\Gamma\kappa_1+1}, \quad k_{2n} = l_{2n} = 0 \quad (n \geqslant 1). \tag{17}$$

Equations (15)–(17) determine the complex potentials (7) and (8). Substituting them in eqns (5) with $z = r\,e^{i\theta}$, we get the polar components of the stresses in the matrix and inclusion.

We are most interested in the interface stresses along the inclusion boundary ($r = a$). They are given by the following explicit formulae:

$$\sigma_{\theta\mathrm{I}} = \frac{\sigma}{2}\left(2 - \frac{\Gamma(\kappa_\mathrm{I}+1)}{2\Gamma+\kappa_\mathrm{II}-1} + \left\{1 - \frac{3(\Gamma-1)}{\Gamma\kappa_\mathrm{I}+1}\right\}\cos 2\theta\right) \tag{18.1}$$

$$\sigma_{\theta\mathrm{II}} = \frac{\sigma}{2}\Gamma(\kappa_\mathrm{I}+1)\left(\frac{1}{2\Gamma+\kappa_\mathrm{II}-1} + \frac{1}{\Gamma\kappa_\mathrm{I}+1}\cos 2\theta\right) \tag{18.2}$$

$$\sigma_{r\mathrm{I}} = \sigma_{r\mathrm{II}} = \frac{\sigma}{2}\Gamma(\kappa_\mathrm{I}+1)\left(\frac{1}{2\Gamma+\kappa_\mathrm{II}-1} - \frac{1}{\Gamma\kappa_\mathrm{I}+1}\cos 2\theta\right) \tag{18.3}$$

$$\tau_{r\theta\mathrm{I}} = \tau_{r\theta\mathrm{II}} = \frac{\sigma}{2}\frac{\Gamma(\kappa_\mathrm{I}+1)}{\Gamma\kappa_\mathrm{I}+1}\sin 2\theta, \tag{18.4}$$

and the maximum interface stresses are given as follows:

$$\sigma_{\theta\mathrm{I},\max} = \begin{cases} \sigma\left(3 - \dfrac{\Gamma(\kappa_\mathrm{I}+1)}{2\Gamma+\kappa_\mathrm{II}-1} - \dfrac{3(\Gamma-1)}{\Gamma\kappa_\mathrm{I}+1}\right) & \left(\text{at } \theta = 0 \text{ if } \Gamma < \dfrac{4}{3-\kappa_\mathrm{I}}\right) \\ \sigma\left(1 - \dfrac{2(\kappa_\mathrm{I}+1)}{8+(3-\kappa_\mathrm{I})(\kappa_\mathrm{II}-1)}\right) & \left(\text{at any } \theta \text{ if } \Gamma = \dfrac{4}{3-\kappa_\mathrm{I}}\right) \\ \dfrac{\sigma}{2}\left(1 - \dfrac{\Gamma(\kappa_\mathrm{I}+1)}{2\Gamma+\kappa_\mathrm{II}-1} + \dfrac{3(\Gamma-1)}{\Gamma\kappa_\mathrm{I}+1}\right) & \left(\text{at } \theta = \dfrac{\pi}{2} \text{ if } \Gamma > \dfrac{4}{3-\kappa_\mathrm{I}}\right) \end{cases} \tag{19.1}$$

$$\sigma_{\theta\mathrm{II},\max} = \frac{\sigma}{2}\Gamma(\kappa_\mathrm{I}+1)\left(\frac{1}{2\Gamma+\kappa_\mathrm{II}-1} + \frac{1}{\Gamma\kappa_\mathrm{I}+1}\right) \quad (\text{at } \theta = 0) \tag{19.2}$$

$$\sigma_{r\mathrm{I},\max} = \sigma_{r\mathrm{II},\max} = \frac{\sigma}{2}\Gamma(\kappa_\mathrm{I}+1)\left(\frac{1}{2\Gamma+\kappa_\mathrm{II}-1} + \frac{1}{\Gamma\kappa_\mathrm{I}+1}\right) \quad \left(\text{at } \theta = \frac{\pi}{2}\right) \tag{19.3}$$

$$\tau_{r\theta\mathrm{I},\max} = \tau_{r\theta\mathrm{II},\max} = \frac{\sigma}{2}\frac{\Gamma(\kappa_\mathrm{I}+1)}{\Gamma\kappa_\mathrm{I}+1} \quad \left(\text{at } \theta = \frac{\pi}{4}\right). \tag{19.4}$$

3. NUMERICAL RESULTS

3.1. *General remarks on numerical analysis and accuracy of results*

Poisson's ratios ν_I and ν_II have only slight effects on the results, and throughout the calculations, we assume $\nu_\mathrm{I} = \nu_\mathrm{II} = 0.3$ in the plane strain case or $\kappa_\mathrm{I} = \kappa_\mathrm{II} = 1.8$.

Numerical results of this problem depend upon the following three parameters:

$$\Gamma = \frac{G_\mathrm{II}}{G_\mathrm{I}} = \frac{E_\mathrm{II}}{E_\mathrm{I}} \quad (\text{if } \nu_\mathrm{I} = \nu_\mathrm{II}) \tag{20}$$

$$\mu = \frac{b}{c}, \quad \lambda = \frac{a}{b}. \tag{21}$$

We are especially interested in all the stress components along the inclusion boundaries, since they are closely related to debonding or cracking of the inclusions. Another important quantity is the effect of inclusions on the apparent tensile stiffness of the solid. In reference

to the latter quantity, the following dimensionless factor C is defined:

$$C = \frac{E^*}{E_0} = \text{tensile stiffness factor} \tag{22.1}$$

$$E^* = \text{apparent Young's modulus of solid with inclusions} \tag{22.2}$$

$$E_0 = \text{Young's modulus of matrix material} = \begin{cases} E_1 & \text{(plane stress)} \\ E_1/(1-\nu_1^2) & \text{(plane strain)} \end{cases} \tag{22.3}$$

where E_1 is Young's modulus of the matrix material measured with thin plate specimens.

The above-defined factor $C = E^*/E_0$ is smaller or larger than unity according to whether $\Gamma < 1$ or $\Gamma > 1$, respectively. As shown later, it depends strongly upon the volume fraction of the inclusions, f, which is defined as follows:

$$f = \text{volume fraction of inclusions} = \frac{\pi a^2}{2bc} = \frac{\pi}{2}\lambda^2\mu. \tag{23}$$

In representing the numerical results we also use the following parameter β instead of Γ:

$$\beta = \frac{\Gamma - 1}{\Gamma + 1} = \frac{G_{II} - G_I}{G_{II} + G_I}$$

$$= \frac{E_{II} - E_I}{E_{II} + E_I} \quad \text{(for the present case when } \nu_I = \nu_{II}\text{)}. \tag{24}$$

Numerical calculations have been carried out for all the possible combinations of the following values of the parameters: $\Gamma = 0, 0.1, 0.2, 0.5, 0.75, 1.5, 2, 3.33, 5, 10, \infty$; $\mu = 0.5, 1/\sqrt{3}, 1, 2$ and $\lambda = 0, 0.1, 0.2, \ldots$. Here the upper limit of λ of course depends on μ. Obviously, λ cannot exceed the values for the extreme cases when some of the adjacent inclusions touch each other, as shown by Figs 3(a), 3(b) and 3(c) depending on the three ranges of μ. This physical upper limit of λ is given as a function of μ in each of the three ranges, and is shown by a kinked dashed curve in Fig. 4. There is also a practical upper limit on λ for which the present analysis gives reliable results with reasonable computing cost. It has been found to be about 80% of the physical limit, that is,

$$\lambda \leqslant \begin{cases} 0.8 & (\mu \leqslant 1/\sqrt{3}) \\ 0.8\sqrt{1+\mu^2}/(2\mu) & (1/\sqrt{3} \leqslant \mu \leqslant \sqrt{3}) \\ 0.8/\mu & (\mu \geqslant \sqrt{3}). \end{cases} \tag{25}$$

This practical upper limit on λ is shown by a kinked solid curve in Fig. 4.

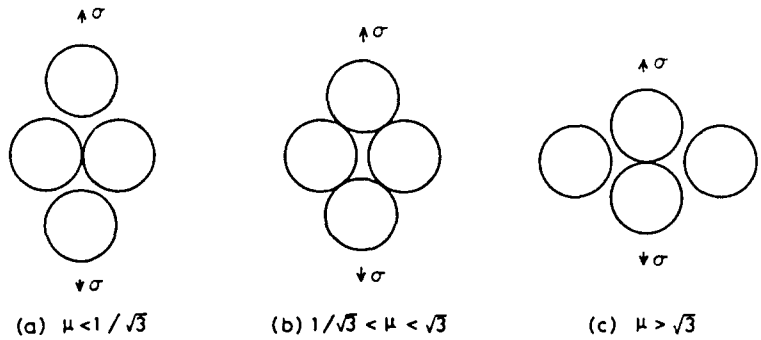

(a) $\mu < 1/\sqrt{3}$ (b) $1/\sqrt{3} < \mu < \sqrt{3}$ (c) $\mu > \sqrt{3}$

Fig. 3. Three extreme cases when adjacent inclusions touch each other.

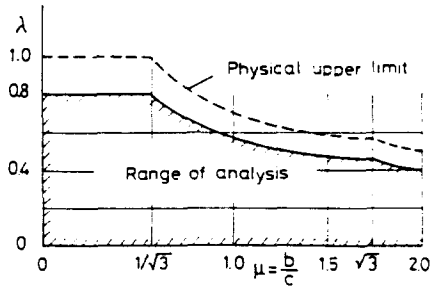

Fig. 4. Range of validity.

For each combination of the three parameters Γ, μ and λ, we have calculated the maximum values of all the interface stress components in domains (I) and (II). They are denoted as $\sigma_{\theta\mathrm{I},\max}$, $\sigma_{\theta\mathrm{II},\max}$, $\sigma_{r,\max}$ ($=\sigma_{r\mathrm{I},\max}=\sigma_{r\mathrm{II},\max}$) and $\tau_{r\theta,\max}$ ($=\tau_{r\theta\mathrm{I},\max}=\tau_{r\theta\mathrm{II},\max}$). These values have been determined by calculating $\sigma_{\theta\mathrm{I}}$, $\sigma_{\theta\mathrm{II}}$, σ_r, $\tau_{r\theta}$ for θ at one degree intervals and taking their largest values. The limiting values for $\lambda \to 0$ are explicitly given by eqns (19.1)–(19.4).

Numerical results by the present analysis are expected to approach the exact values with increasing number of the boundary elements. As an example, Table 1 gives the results for the case of $\Gamma = 0.5$, $\mu = 1$ and $\lambda = 0.5$ calculated by using triangular unit regions with 4, 8, 12 and 16 elements. We find rapid convergence of the numerical results with increasing values of N, and the errors seem less than 0.2% even for $N = 4$. This procedure has been used to confirm the high accuracy of all the numerical results to be discussed in the following section.

3.2. *Effects of parameters on interface stresses and tensile stiffness*

It would consume an enormous number of pages to present here all the numerical results calculated for 330 combinations of the parameters shown in the preceding section. Moreover, when the values for some other combinations of Γ, μ and λ are required, we have to make interpolations with respect to these three parameters, causing considerable errors in the results. For this reason, we have established reliable formulae for the five quantities treated and referred to in Table 1. Before going to these formulae, let's make some comments on the general trends of the numerical results for typical cases of the parameters.

We begin with the stresses in the limiting case of $\lambda \to 0$. They are given by eqns (19.1)–(19.4), and the results for the present Poisson's ratios ($\nu_{\mathrm{I}} = \nu_{\mathrm{II}} = 0.3$ in plane strain) are plotted against $\Gamma = G_{\mathrm{II}}/G_{\mathrm{I}}$ in Fig. 5. In the range $\Gamma < 3.33$, $\sigma_{\theta\mathrm{I},\max}$ occurs at $\theta = 0$ and decreases with increasing values of Γ, but when $\Gamma > 3.33$, $\sigma_{\theta\mathrm{I},\max}$ takes place at $\theta = 90°$ and increases with increasing values of Γ towards the limiting value for $\Gamma \to \infty$. The special case of $\Gamma = 3.33$ gives "the neutral inclusion" for which $\sigma_{\theta\mathrm{I},\max}$ is constant, independent of θ. The $\sigma_{\theta\mathrm{I},\max}$ vs Γ relation is thus given by a kinked curve. $\sigma_{\theta\mathrm{II},\max}$ is equal to $\sigma_{r,\max}$ independent of Γ, though they occur at different points $\theta = 0°$ and $\theta = 90°$, respectively. $\tau_{r\theta,\max}$ takes place at $\theta = 45°$ for any values of Γ. The latter three stresses increase monotonically with increasing values of Γ, and approach their limiting values for $\Gamma \to \infty$ shown by chained lines.

Table 1. Variations of results with number of subdivisions ($\Gamma = 0.5$, $\mu = 1$ and $\lambda = 0.5$, triangular region)

N	$\sigma_{\theta\mathrm{I},\max}/\sigma$	$\sigma_{\theta\mathrm{II},\max}/\sigma$	$\sigma_{r,\max}/\sigma$	$\tau_{r\theta,\max}/\sigma$	E^*/E_0
4	1.63259	0.81242	0.89456	0.45560	0.74053
8	1.63451	0.81360	0.89328	0.45597	0.74002
12	1.63450	0.81360	0.89323	0.45597	0.74001
16	1.63450	0.81360	0.89323	0.45597	0.74001

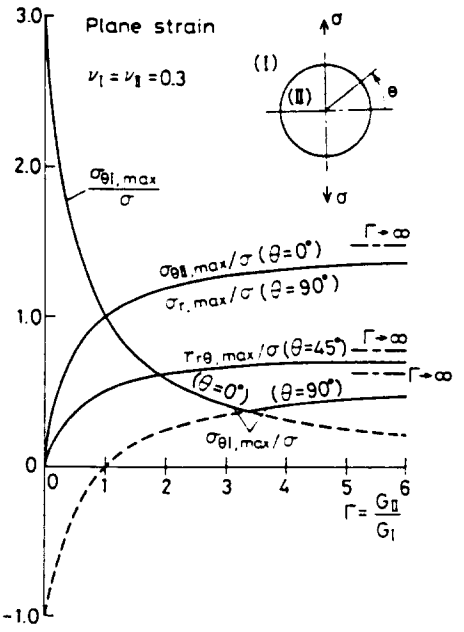

Fig. 5. Maximum interface stresses for a single inclusion (plane strain, $\nu_I = \nu_{II} = 0.3$).

As for the magnitudes of these maximum interface stresses, we have the following relations depending on three ranges of Γ:

$$\sigma_{\theta I,max} > \sigma_{\theta II,max} = \sigma_{r,max} > \tau_{r\theta,max} \quad (\text{for } 0 < \Gamma < 1) \tag{26.1}$$

$$\sigma_{\theta II,max} = \sigma_{r,max} > \sigma_{\theta I,max} > \tau_{r\theta,max} \quad (\text{for } 1 < \Gamma < 1.94) \tag{26.2}$$

$$\sigma_{\theta II,max} = \sigma_{r,max} > \tau_{r\theta,max} > \sigma_{\theta I,max} \quad (\text{for } 1.94 < \Gamma). \tag{26.3}$$

The above behavior for extremely small inclusions is nearly maintained in the results for zig-zag inclusions shown by Figs 6–9. Solid curves in these figures show the analytical

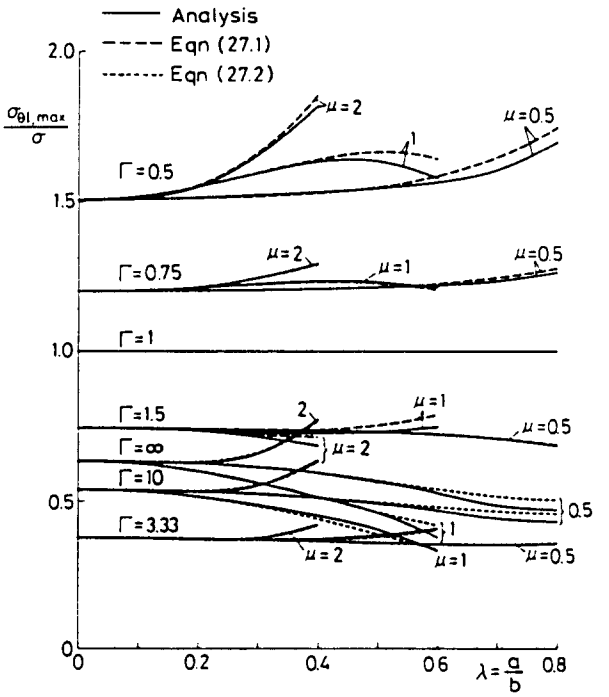

Fig. 6. $\sigma_{\theta I,max}/\sigma$.

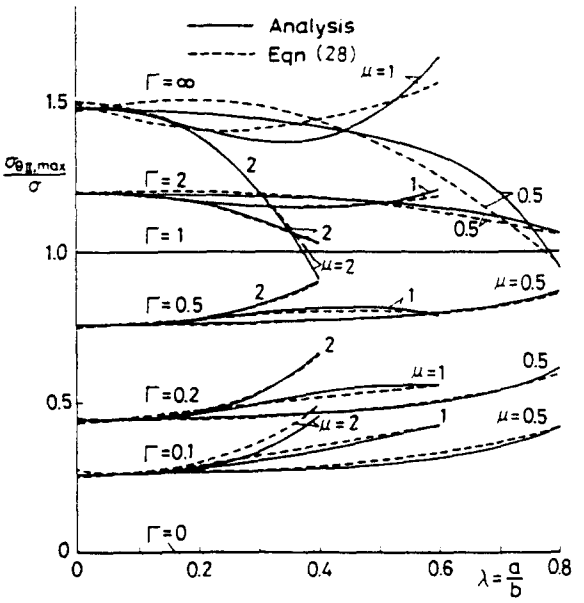

Fig. 7. $\sigma_{\theta\theta,max}/\sigma$.

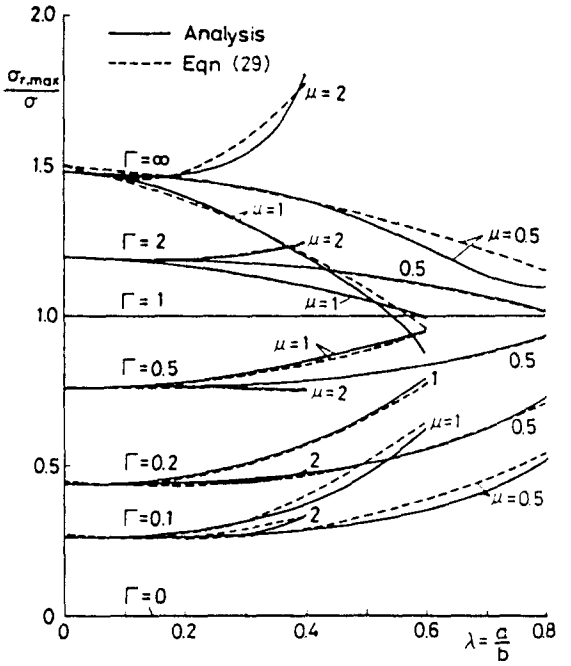

Fig. 8. $\sigma_{r,max}/\sigma$.

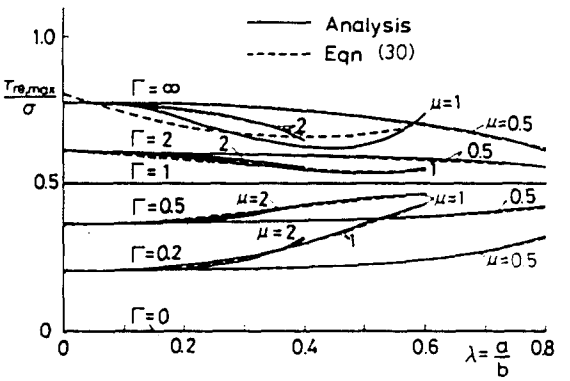

Fig. 9. $\tau_{r\theta,max}/\sigma$.

values of the maximum interface stresses for typical values of the parameters. As is seen in Fig. 6, $\sigma_{\theta\mathrm{I},\max}$ decreases with increasing values of Γ for fixed values of μ and λ if $\Gamma < 3.33$, but the trend is reversed when Γ exceeds 3.33. The maxima of the other stress components tend to increase monotonically when Γ increases, as shown by Figs 7–9, but the effect of μ depends on Γ and λ, and is not so consistent as that of Γ.

The locations θ of these stress maxima are also important, since they give useful information on the initiation points of debonding or fracture of the inclusions. They are nearly the same as shown in parentheses in eqns (19.1)–(19.4) and in Fig. 5 for a single inclusion. In the special case of a square array [Fig. 12(a)], the values of θ for $\sigma_{\theta\mathrm{I},\max}$, $\sigma_{\theta\mathrm{II},\max}$ and $\sigma_{r,\max}$ are the same as for a single inclusion except for the range $\Gamma \leqslant 0.2$ and $\lambda \geqslant 0.5$ where θ takes some values between 0° and 90°. As for $\tau_{r\theta,\max}$, θ is 45° if $\lambda < 0.3$, but for larger values of λ, θ increases or decreases from 45° according to whether $\Gamma < 1$ or $\Gamma > 1$. Further discussions will be made in Section 3.4 for special arrays of inclusions.

Figure 10 shows the stiffness factor E^*/E_0 plotted against λ in a similar manner to that for the stresses. Figure 11 is another diagram for E^*/E_0 in which the abscissa λ is replaced by f, the volume fraction of the inclusions defined by eqn (23). We find that the E^*/E_0 vs f curves for any fixed value of Γ in Fig. 11 lie within a band considerably narrower than the corresponding E^*/E_0 vs λ curves in Fig. 10. In other words, the stiffness factor E^*/E_0 is only slightly affected by the parameter f, and it is nearly a function of f. A zig-zag array of circular inclusions may be regarded as a typical model of randomly distributed inclusions in solids. Therefore, the above observation seems to suggest a strong f-dependence of the tensile stiffness of actual solids.

3.3. *Approximate formulae for stresses and tensile stiffness factor*

In this section we propose reliable formulae for the five quantities discussed above. They are given as power series involving three parameters Γ, μ, λ or their substitutes, and their coefficients are determined so as to give the best fit to the analytical values in the least-squares sense. The accuracy of this kind of formulae is improved by taking higher order terms, but they can be truncated at the second- to the fourth-order terms for each parameter without substantial loss of accuracy.

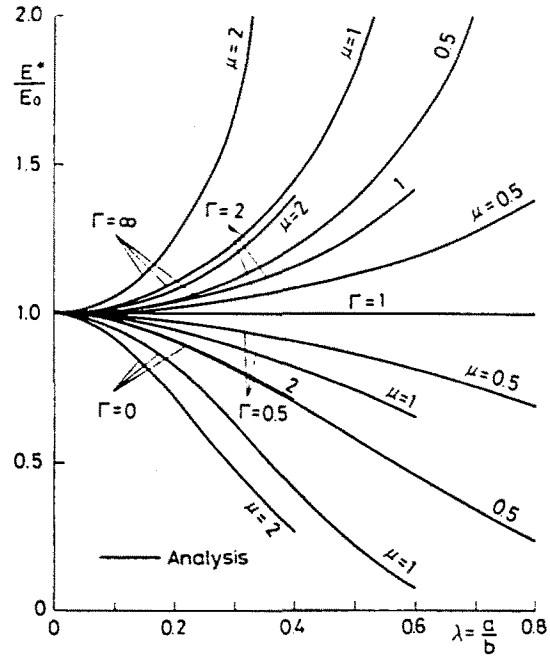

Fig. 10. E^*/E_0 vs λ relations for various Γ and μ.

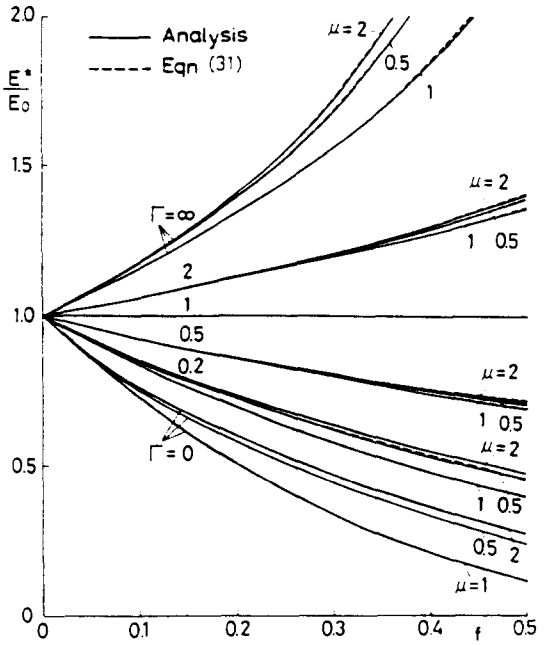

Fig. 11. E^*/E_0 vs f relations for various Γ and μ.

In establishing these formulae, we consider the following aspects.

(i) For solids without inclusions ($\Gamma = 1$), we must have $\sigma_{\theta\mathrm{I},\max} = \sigma_{\theta\mathrm{II},\max} = \sigma_{r,\max} = \sigma$, $\tau_{r\theta,\max} = \sigma/2$ and $E^*/E_0 = 1$. These requirements are satisfied by superposing positive power series of $(\Gamma - 1)$ on the above known values for $\Gamma = 1$.

(ii) The five quantities treated must remain finite in both the extreme cases, i.e. when $\Gamma \to 0$ and $\Gamma \to \infty$. This requirement is satisfied by replacing the variable introduced above, $(\Gamma - 1)$, by $(\Gamma - 1)/(\Gamma + A)$, where A is a positive constant. It is reasonable to determine this constant so as to give the best fit to the analytical values. The optimum value of A has been found to be around unity by trial-and-error, and we have decided to use a new rigidity parameter β defined by eqn (24).

(iii) As for parameters other than Γ, μ and λ are convenient for the stresses, but μ and f are more suitable for the stiffness factor E^*/E_0 referring to the discussions regarding Figs 10 and 11.

Taking the above into consideration, we have fitted power series to the analytical values including those for the limiting case of $\lambda \to 0$ calculated from eqns (19.1)–(19.4). The resulting expressions for the stresses and stiffness factor are as follows:

$$\frac{(\sigma_{\theta\mathrm{I},\max})_{\Gamma=3.33}}{\sigma} = 1 - 1.353\beta + 0.450\beta^2 - 0.186\beta^3 + \sum_{l=0}^{2}\sum_{m=0}^{2}\sum_{n=0}^{2} A_{lmn}^{(\theta\mathrm{I})}\lambda^{l+2}\mu^m\beta^{n+1} \tag{27.1}$$

$$\frac{(\sigma_{\theta\mathrm{I},\max})_{\Gamma=3.33}}{\sigma} = 0.784\beta - 0.177\beta^2 + 0.026\beta^3 + \sum_{l=0}^{2}\sum_{m=0}^{2}\sum_{n=0}^{2} A_{lmn}^{(\theta\mathrm{I})}\lambda^{l+2}\mu^m\beta^{n+1} \tag{27.2}$$

$$\frac{\sigma_{\theta\mathrm{II},\max}}{\sigma} = 1 + \sum_{l=0}^{2}\sum_{m=0}^{2}\sum_{n=0}^{2} B_{lmn}^{(\theta\mathrm{II})}\lambda^{l}\mu^m\beta^{n+1} \tag{28}$$

$$\frac{\sigma_{r,\max}}{\sigma} = 1 + \sum_{l=0}^{2}\sum_{m=0}^{2}\sum_{n=0}^{2} C_{lmn}^{(r)}\lambda^{l}\mu^m\beta^{n+1} \tag{29}$$

$$\frac{\tau_{r\theta,\max}}{\sigma} = 0.5 + \sum_{l=0}^{2}\sum_{m=0}^{2}\sum_{n=0}^{2} D_{lmn}^{(r\theta)}\lambda^{l}\mu^m\beta^{n+1} \tag{30}$$

$$C = \frac{E^*}{E_0} = 1 + \sum_{l=0}^{2} \sum_{m=0}^{2} \sum_{n=0}^{2} E_{lmn} f^{l+1} \mu^m \beta^{n+1}. \tag{31}$$

Values of the coefficients in eqns (27.1)–(31) are shown in Table 2. For $\sigma_{\theta 1,\max}/\sigma$ only, different formulae are proposed in two ranges $\Gamma \leqslant 3.33$ and $\Gamma \geqslant 3.33$, considering its behavior as shown in Fig. 6.

Equations (27.1)–(30) give reliable values for $\Gamma \geqslant 0.1$ ($1 > \beta \geqslant -0.82$), $0.5 \leqslant \mu \leqslant 2$ and for λ within the hatched area of Fig. 4. Equation (31) is valid in the same ranges of Γ and μ and for $f \leqslant 0.5$. The bottom row of Table 2 shows the mean per cent errors for these formulae. They are between 1.3% and 4% for the stresses, and less than 0.2% for the stiffness factor.

Values from the above formulae are also shown in Figs 6–9 and 11 by dashed or dotted curves. We find these formulae to be fairly accurate. In Fig. 6 for $\sigma_{\theta 1,\max}/\sigma$, curves for $\Gamma < 0.5$ are not shown, but eqn (27.1) is valid for $\Gamma \geqslant 0.1$ as mentioned above.

3.4. *Special arrays of inclusions*

We are most interested in the special arrays of inclusions as shown in Figs 12(a) and 12(b). Analytical values of the maximum interface stresses and stiffness factor are given by solid curves in Figs 13–17 for the square array and in Figs 18–22 for the equilateral triangular array. The locations θ of the maximum interface stresses are usually the same as shown in parentheses in eqns (19.1)–(19.4) for a single inclusion, and are shown at the tops of the corresponding figures. As for the exceptional cases, values of θ are also given in parentheses in the figures. The curve for $\Gamma = 0.1$ in Fig. 13 is shown to fluctuate in inclination, since θ begins to increase from zero around $\lambda \doteqdot 0.5$. For comparison, values of $\sigma_{\theta 1}/\sigma$ at $\theta = 0$ are also given by thin solid curves in Figs 13 and 18.

For these special arrays, we can establish two-parametric formulae which are more reliable than the three-parametric formulae (27.1)–(31). They are the following equations

Table 2. Coefficients in eqns (27.1)–(31) (plane strain, $\nu_1 = \nu_{11} = 0.3$)

l	m	n	$A^{(\theta 1)}_{lmn}$		$B^{(\theta\theta)}_{lmn}$	$C^{(r)}_{lmn}$	$D^{(r\theta)}_{lmn}$	E_{lmn}
			$\Gamma \leq 3.33$	$\Gamma \geq 3.33$				
0	0	0	2.7966	0.4610	0.5458	0.6131	0.3126	1.9864
0	0	1	-6.5293	-2.6378	-0.2780	-0.2307	-0.1348	-0.5765
0	0	2	2.8987	3.7098	0.1068	0.1044	0.0383	0.1901
0	1	0	-8.3745	-1.4372	0.1903	0.0441	0.1043	0.0253
0	1	1	17.043	6.3568	0.0494	0.0135	0.0840	-0.1984
0	1	2	-5.3930	-8.7575	-0.0655	-0.0228	-0.0470	0.1166
0	2	0	3.4580	0.7992	-0.0703	-0.0128	-0.0420	-0.0113
0	2	1	-6.9820	-3.1490	-0.0141	-0.0082	-0.0342	0.0854
0	2	2	1.6925	3.7658	0.0259	0.0044	0.0215	-0.0392
1	0	0	-4.9090	-28.840	2.4582	0.7494	1.1971	0.2097
1	0	1	-4.9648	79.324	1.1515	0.0495	0.9533	6.3089
1	0	2	24.091	-52.771	-0.6819	-0.6333	-0.4201	-3.7038
1	1	0	17.778	72.011	-5.3514	-1.0697	-2.8198	-0.3669
1	1	1	5.9390	-196.16	-2.3327	-0.6948	-2.5935	-8.5739
1	1	2	-66.171	127.40	1.8348	1.0225	1.3545	3.8481
1	2	0	-11.023	-32.372	2.1258	0.2480	1.1735	0.1656
1	2	1	3.4860	85.618	0.8437	0.1923	1.0150	3.4263
1	2	2	30.372	-54.150	-0.7184	-0.3029	-0.5843	-1.7020
2	0	0	-6.1295	21.943	-5.6071	0.4256	-1.3977	-0.5777
2	0	1	32.099	-56.474	-3.5681	0.3494	-2.3343	-2.9757
2	0	2	-34.277	37.641	1.3259	1.1198	0.5995	11.646
2	1	0	7.4438	-55.636	12.145	-4.4411	2.8640	1.0053
2	1	1	-73.724	139.18	7.6228	-0.7173	5.9969	7.7313
2	1	2	100.39	-90.200	-3.4236	-1.0536	-1.8996	-16.160
2	2	0	2.6645	29.981	-5.5516	2.4770	-1.4947	-0.4554
2	2	1	30.636	-68.245	-3.0918	0.9338	-2.2826	-2.8784
2	2	2	-64.172	42.509	1.4630	0.1348	0.8950	7.0315
Mean error (%)			4.0	1.6	1.5	1.3	1.7	0.2

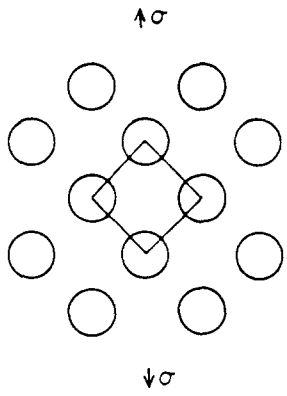

Fig. 12(a). Square array of inclusions ($\mu = 1$).

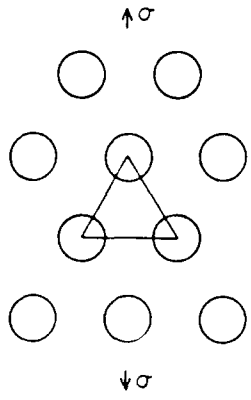

Fig. 12(b). Equilateral triangular array of inclusions ($\mu = 1$, $\sqrt{3}$).

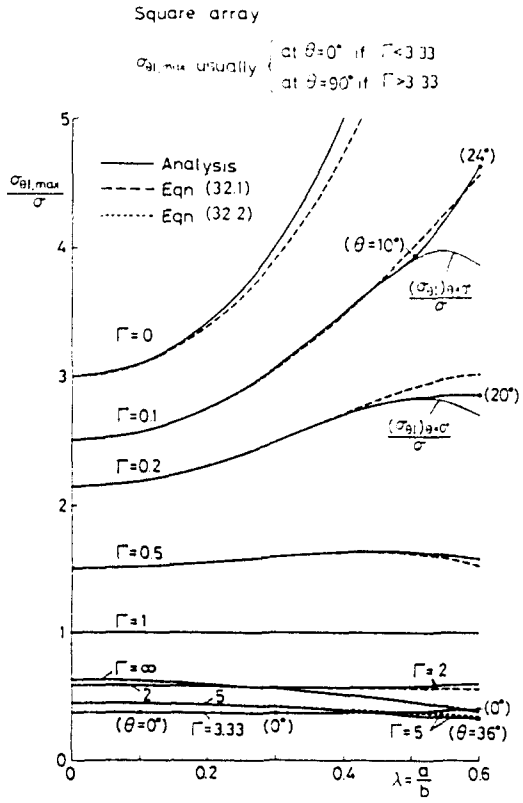

Fig. 13. $\sigma_{\theta 1,\max}/\sigma$ for square array ($\mu = 1$).

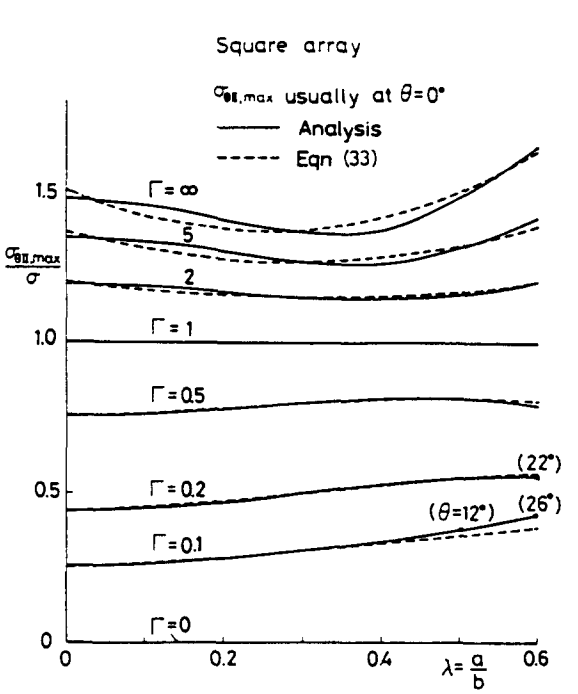

Fig. 14. $\sigma_{\theta\theta,max}/\sigma$ for square array ($\mu = 1$).

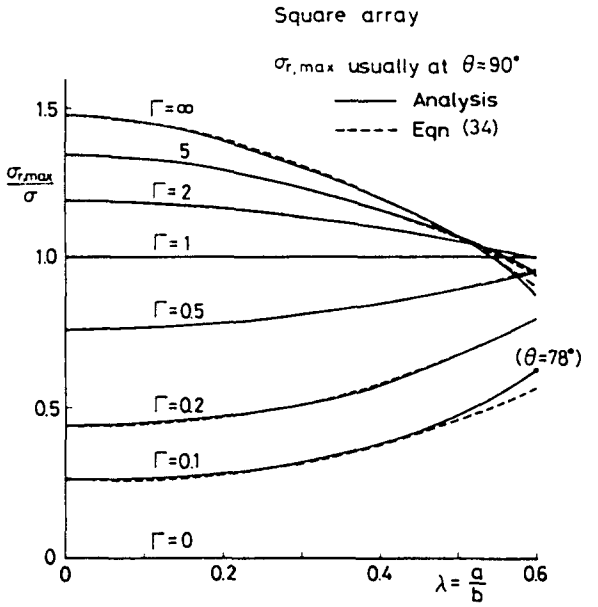

Fig. 15. $\sigma_{r,max}/\sigma$ for square array ($\mu = 1$).

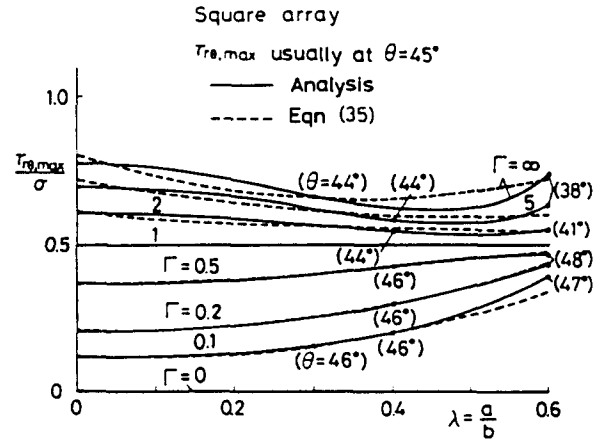

Fig. 16. $\tau_{r\theta,max}/\sigma$ for square array ($\mu = 1$).

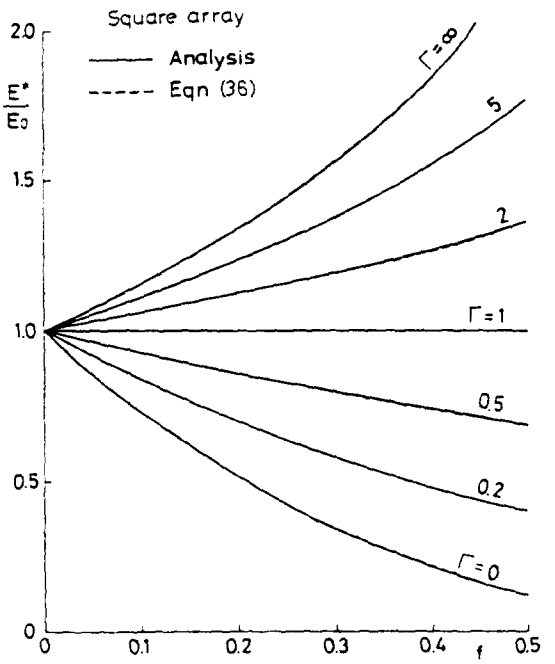

Fig. 17. E^*/E_0 for square array ($\mu = 1$).

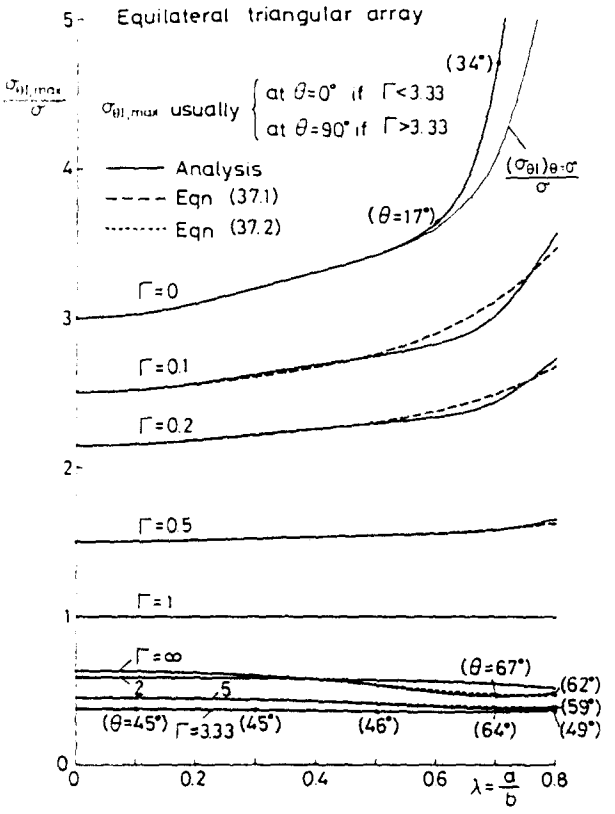

Fig. 18. $\sigma_{\theta 1,\max}/\sigma$ for equilateral triangular array ($\mu = 1/\sqrt{3}$).

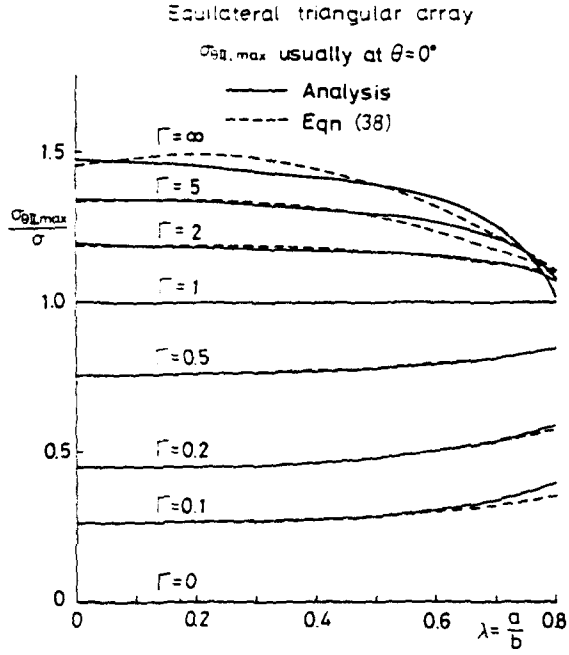

Fig. 19. $\sigma_{\theta\theta,max}$ σ for equilateral triangular array ($\mu = 1\sqrt{3}$).

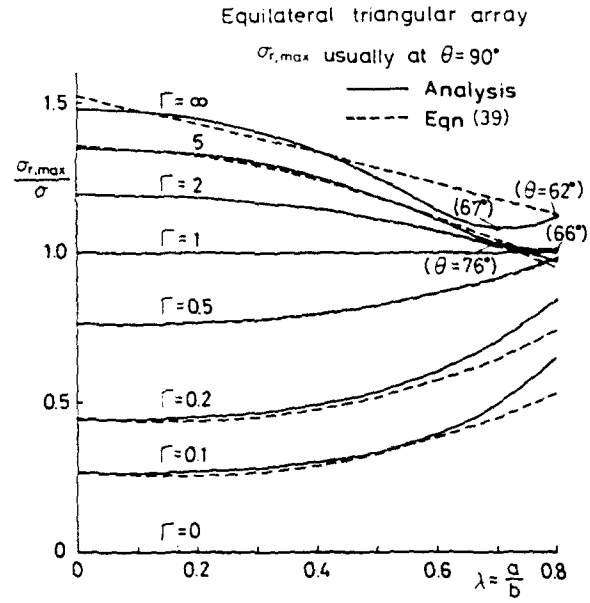

Fig. 20. $\sigma_{r,max}$ σ for equilateral triangular array ($\mu = 1\sqrt{3}$).

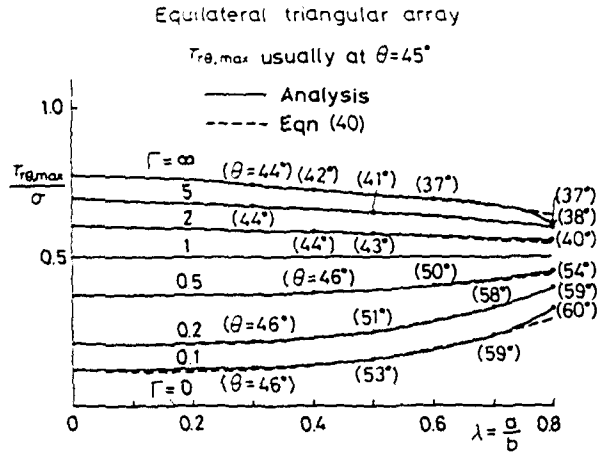

Fig. 21. $\tau_{r\theta,max}$ σ for equilateral triangular array ($\mu = 1\sqrt{3}$).

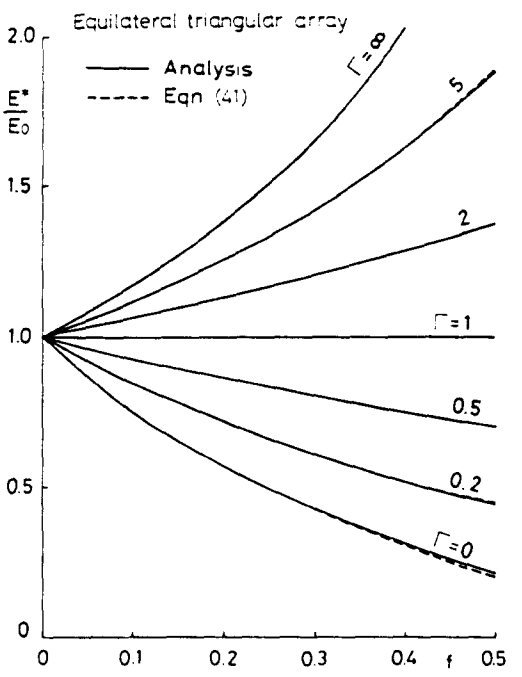

Fig. 22. E^*/E_0 for equilateral triangular array ($\mu = 1/3$).

(32.1)–(36) for the square array valid in the range $\lambda \leqslant 0.6$, and equations (37.1)–(41) for the equilateral triangular array valid in the range $\lambda \leqslant 0.8$. $\sigma_{\theta\mathrm{L,max}}$ is represented by different formulae in two ranges $\Gamma \leqslant 3.33$ and $\Gamma \geqslant 3.33$. Other quantities are fitted to single formulae in the whole range of Γ. The accuracies of eqns (27.1)–(41) are reasonable, as seen from the mean per cent errors given in parentheses with each of the formulae.

Square array of inclusions ($\mu = 1$):

$$\frac{(\sigma_{\theta\mathrm{L,max}})_{\Gamma \leqslant 3.33}}{\sigma} = 1 + \beta[-1.356 + 0.423\beta - 0.149\beta^2 + 0.070\beta^3 + \lambda^2(-2.043 + 3.436\beta - 1.330\beta^2 + 2.538\beta^3) + \lambda^3(0.854 + 8.282\beta - 10.563\beta^2 - 18.728\beta^3) + \lambda^4(4.426 - 27.543\beta + 14.574\beta^2 + 58.076\beta^3)]$$

(mean error 4.0%) (32.1)

$$\frac{(\sigma_{\theta\mathrm{L,max}})_{\Gamma \geqslant 3.33}}{\sigma} = \beta[0.784 - 0.177\beta + 0.026\beta^2 + \lambda^2(0.271 - 0.667\beta - 0.596\beta^2) + \lambda^3(7.164 - 21.227\beta + 14.915\beta^2) + \lambda^4(2.216 - 1.817\beta - 0.922\beta^2)]$$

(mean error 1.4%) (32.2)

$$\frac{\sigma_{\theta\mathrm{LL,max}}}{\sigma} = 1 + \beta[0.675 - 0.210\beta + 0.052\beta^2 - 0.033\beta^3 + 0.028\beta^4 + \lambda(-0.943 - 0.482\beta + 0.722\beta^2 - 0.102\beta^3 - 0.322\beta^4) + \lambda^2(1.348 + 1.526\beta - 1.616\beta^2 - 0.362\beta^3 + 1.311\beta^4)]$$

(mean error 1.3%) (33)

$$+\beta[0.649-0.211\beta+0.050\beta^2-0.048\beta^3+0.040\beta^4$$
$$+\lambda(-0.179-0.398\beta+0.789\beta^2+0.304\beta^3-0.652\beta^4)$$
$$+\lambda^2(-1.310+0.990\beta-1.768\beta^2-1.603\beta^3+2.311\beta^4)]$$

(mean error 0.7%) (34)

$$^{ax} = 0.5+\beta[0.376-0.077\beta+0.002\beta^2-0.018\beta^3+0.025\beta^4$$
$$+\lambda(-0.486-0.734\beta+0.699\beta^2+0.277\beta^3-0.618\beta^4)$$
$$+\lambda^2(0.067+1.984\beta-1.605\beta^2-1.307\beta^3+2.067\beta^4)]$$

(mean error 2.1%) (35)

$$+f\beta[1.996-0.726\beta+0.244\beta^2+f(0.027+1.660\beta-0.876\beta^2)$$
$$+f^2(-0.054-0.154\beta-0.634\beta^2)+f^3(0.006+2.362\beta+3.861\beta^2)]$$

(mean error 0.1%). (36)

:ral triangular array of inclusions ($\mu = 1/\sqrt{3}$):

$$\frac{(\sigma_{\theta\theta,\max})_{\text{I}\ldots\text{III}}}{\sigma} = 1+\beta[-1.356+0.423\beta-0.149\beta^2+0.070\beta^3$$
$$+\lambda^2(-0.825+1.534\beta-0.463\beta^2+0.202\beta^3)$$
$$+\lambda^3(1.810-3.038\beta-0.466\beta^2-2.485\beta^3)$$
$$+\lambda^4(-1.706+1.592\beta+1.396\beta^2+6.578\beta^3)]$$

(mean error 2.0%) (37.1)

$$\frac{(\sigma_{\theta\theta,\max})_{\text{I}\ldots\text{III}}}{\sigma} = \beta[0.784-0.177\beta+0.026\beta^2+\lambda^2(-0.062-0.099\beta+0.028\beta^2)$$
$$+\lambda^3(0.997-2.814\beta+0.766\beta^2)+\lambda^4(0.327-0.282\beta+1.069\beta^2)]$$

(mean error 0.9%) (37.2)

$$\frac{\sigma_{\theta\theta,\max}}{\sigma} = 1+\beta[0.629-0.231\beta+0.069\beta^2-0.046\beta^3+0.024\beta^4$$
$$+\lambda(0.132+0.089\beta+0.212\beta^2+0.112\beta^3-0.135\beta^4)$$
$$+\lambda^2(-0.562-0.169\beta-0.359\beta^2-0.365\beta^3+0.367\beta^4)]$$

(mean error 1.1%) (38)

$$\frac{\sigma_{r,\max}}{\sigma} = 1+\beta[0.634-0.191\beta+0.074\beta^2-0.052\beta^3+0.046\beta^4$$
$$+\lambda(0.235-0.501\beta+0.104\beta^2+0.266\beta^3-0.524\beta^4)$$
$$^{2}(-1.347+0.820\beta-0.017\beta^2-0.846\beta^3+1.240\beta^4)]$$

(mean error 1.4%) (39)

$$\frac{\tau_{rr,\max}}{\sigma} = 0.5+\beta[0.360-0.081\beta-0.009\beta^2-0.029\beta^3+0.037\beta^4$$
$$+\lambda(-0.053-0.401\beta+0.586\beta^2+0.358\beta^3-0.553\beta^4)$$
$$+\lambda^2(-0.214+0.817\beta-1.024\beta^2-0.858\beta^3+1.150\beta^4)]$$
(mean error 1.3%) (40)

$$C=\frac{E^*}{E_0} = 1+f\beta[1.997-0.721\beta+0.242\beta^2+f(0.010+3.478\beta-1.838\beta^2)$$
$$+f^2(0.078-3.614\beta+3.298\beta^2)+f^3(-0.245+5.260\beta+1.881\beta^2)]$$
(mean error 0.2%). (41)

Dashed and dotted curves in Figs 13–22 show the results from formulae (32.1)–(41), and we find these formulae to be highly accurate. In particular, eqns (36) and (41) for E^*/E_0 give highly accurate values, as seen in Figs 17 and 22.

Finally, the numerical values for E^*/E_0 for these special arrays are given in Tables 3 and 4, taking λ instead of f as the geometric parameter.

4. CONCLUDING REMARKS

A theoretical analysis was performed for an infinite zig-zag array of circular inclusions in a two-dimensional solid under uniaxial tension. Computations were carried out for 330 combinations of mechanical and geometric parameters, and the maximum interface stresses and tensile stiffness of the solid were calculated.

For any fixed values of G_{II}/G_I, the tensile stiffness factor of the solid is little affected by the distribution pattern of the inclusions, and is nearly a function of f, the volume fraction of the inclusions. This seems to suggest a strong f-dependence of the tensile stiffness of actual solids with randomly distributed inclusions.

Results for the maximum interface stresses and the tensile stiffness factor were fitted to power series formulae. They enabled us to obtain reliable values for arbitrary combinations of the parameters.

Table 3. E^*/E_0 for square array of inclusions

λ \ Γ	0	0.2	0.5	1.5	2.0	5.0	∞
0.1	0.954	0.973	0.988	1.006	1.010	1.017	1.024
0.2	0.823	0.896	0.954	1.024	1.038	1.070	1.097
0.3	0.631	0.777	0.898	1.054	1.087	1.163	1.229
0.4	0.414	0.631	0.824	1.098	1.160	1.308	1.443
0.5	0.216	0.482	0.740	1.158	1.264	1.535	1.815
0.6	0.072	0.354	0.654	1.240	1.417	1.943	2.653

Table 4. E^*/E_0 for equilateral triangular array of inclusions

λ \ Γ	0	0.2	0.5	1.5	2.0	5.0	∞
0.1	0.973	0.985	0.993	1.003	1.006	1.010	1.014
0.2	0.899	0.940	0.973	1.014	1.022	1.041	1.057
0.3	0.790	0.872	0.941	1.031	1.051	1.095	1.134
0.4	0.662	0.787	0.899	1.057	1.093	1.178	1.257
0.5	0.529	0.691	0.847	1.090	1.150	1.298	1.444
0.6	0.397	0.590	0.789	1.134	1.226	1.472	1.742
0.7	0.268	0.487	0.727	1.188	1.326	1.731	2.256
0.8	0.146	0.388	0.661	1.255	1.457	2.134	3.284

REFERENCES

Isida, M. (1971). Effect of width and length on stress intensity factors of internally cracked plates under various boundary conditions. *Int. J. Frac. Mech.* **7**, 301–316.

Isida, M. (1978). A new procedure of the body force method with applications to fracture mechanics. *Proc. 1st Int. Conf. on Numerical Methods in Fracture Mechanics*, Swansea, pp. 81–94.

Isida, M. and Igawa, H. (1991). Analysis of a zig-zag array of circular holes in an infinite solid under uniaxial tension. *Int. J. Solids Structures* **27**(7), 849–864.

Isida, M. and Noguchi, H. (1984). Tension of a plate containing an embedded elliptical crack. *Engng Fracture Mech.* **20**, 387–408.

Timoshenko, S. and Goodier, J. N. (1951). *Theory of Elasticity*, 2nd Edn. McGraw-Hill, New York.